Supporting Information

Memmesheimer 10.1073/pnas.0909615107

SI Section A: Discussion Accompanying Figs. S1–S6

Fig. S1. In agreement with previous studies (1–3), I find no transiently increased activity with high-frequency oscillations in random networks with linear coupling. Fig. S1*A* shows a simulation of the same network and with the same initial conditions as in Fig. 1*A*, up to the dendritic modulation function [here: $\sigma(\varepsilon) = \varepsilon$]. After external stimulation of an initial group, the group size of the initiated chain decreases quickly and in nearly every step. This decrease can be understood by considering the transition matrix (Fig. S1*B*): There is no range of amplification; short-lived, enhanced propagation of synchrony does not occur. With high probability, response pulses are smaller than preceding pulses, in particular for larger pulse sizes. The analytically and semianalytically derived mean response pulse sizes show a small, increasing deviation from the numerical estimations for larger initial pulse sizes: In the analytical computations, I assume that neurons contributing a spike to a pulse will not contribute a spike to the succeeding pulse because of their relative refractoriness. This assumption is not valid for very large pulses generating very strong inputs.

Fig. S2. Fig. S2 shows that short-lived, enhanced propagation of synchrony in front of a background of irregular activity occurs robustly in supralinearly coupled networks in contrast to linearly coupled networks. The generation depends on the networks' coupling strengths, which are parameterized by the mean total excitatory coupling strength $\bar{\varepsilon}_{\mathrm{Ex,tot}}$ and by the mean total inhibitory coupling strength $\bar{\varepsilon}_{\mathrm{In,tot}}$ in the network. In each trial, chains of propagating synchrony are initiated by external stimulation of a group of $g'_0 = 45$ neurons. In Fig. S2, blue indicates short-lived, enhanced propagation of synchrony (at least one pulse is larger than $2g'_0$, and pulse sizes reach the level of spontaneous synchronization within at least 10 steps). Green indicates stable propagation of synchrony (group size stays above the level of spontaneous synchronization for at least 10 steps, practically not present). Red shows unstable background activity (level of spontaneous synchronization is larger than or equal to g'_0, often indicating epileptiform network activity). An event of short-lived, enhanced propagation of synchrony may (and, depending on the network parameters, often does) consist of only a few synchronous pulses.

In Fig. S2*A*, sharp transitions in the frequency of occurrence of enhanced propagation of synchrony (or epileptiform activity) are present in the direction of changed excitation strength. These sharp transitions are a consequence of the homogeneous coupling strengths and the sharp onset of supralinear amplification. They are found at $\bar{\varepsilon}_{\mathrm{Ex,tot}} = 47.5$ mV, $\bar{\varepsilon}_{\mathrm{Ex,tot}} = 51.\overline{81}$ mV, and $\bar{\varepsilon}_{\mathrm{Ex,tot}} = 57$ mV, corresponding to the transition from 13 to 12, from 12 to 11, and from 11 to 10 excitatory inputs needed for the generation of a dendritic spike. The transitions are smoothed, e.g., when considering an inhomogeneous coupling strength distribution, as shown in Fig. S2*C*. Here, individual coupling strengths are distributed uniformly in an interval 0.03 mV in width around the mean strength. The results from simulations of linearly coupled networks (Fig. S2*D*) are qualitatively unchanged.

The parameters range from $\bar{\varepsilon}_{\mathrm{Ex,tot}} = 42$ mV to $\bar{\varepsilon}_{\mathrm{Ex,tot}} = 63$ mV and from $\bar{\varepsilon}_{\mathrm{In,tot}} = -42$ mV to $\bar{\varepsilon}_{\mathrm{In,tot}} = -63$ mV in steps of 0.375 mV (40 simulations each). For networks with supralinear dendritic interactions, a larger initial group size also can generate short-lived, enhanced propagation of synchrony in regions with smaller $\bar{\varepsilon}_{\mathrm{Ex,tot}}$, because the range of nonlinear enhancement (Fig. 1) is shifted to larger pulse sizes and then can be reached. In the linearly coupled network, because of the shape of the transition matrix (Fig. S1), short lived, enhanced propagation of synchrony does not occur. The shape might be different in very different parameter regimes (4).

Fig. S3. Fig. S3 shows the typical dynamics of different single neurons during an event of increased activity and high-frequency oscillations in model 2. Fig. S3*A* displays the dynamics of an excitatory neuron which does not participate in the event, Fig. S3*B* displays the dynamics of an excitatory neuron which participates in the event, and Fig. S3*C* shows the dynamics of an inhibitory neuron, each during the event displayed in Fig. 3*A*. Excitation and inhibition are enhanced in excitatory neurons during events (Fig. S3 *A* and *B*, second and third rows) because of the increased firing rate in the excitatory and inhibitory neuron population. Excitation in inhibitory neurons is enhanced; the increase of inhibition is comparatively small because of the very sparse recurrent connectivity within the inhibitory neuron population and their comparatively small number (larger excursions in the second row of Fig. S3*C* are caused by external inputs). For the excitatory neurons, in the lowest row, the times at which the soma responds to a dendritic spike are marked in green. In the nonparticipating neuron (Fig. S3*A*), a dendritic spike is generated that induces a current pulse and a steep depolarization of the somatic potential (spikelet) but no somatic spike, because the soma was not sufficiently depolarized previously. This subthreshold excitation is a consequence of the size of the current pulse chosen in agreement with experimental findings on supralinear dendrites (5–7). Different experimental conditions (e.g., de-inactivated sodium channels in proximal dendrites) or simultaneous dendritic spike arrivals from multiple dendritic compartments might lead to stronger depolarizations and to reliable somatic spike generation. In the participating neuron (Fig. S3*B*), the first dendritic spike generates a somatic spike. The inhibitory neurons spike with high rate around 200 Hz (*Bottom* row in Fig. S3*C*) because of their fast-response properties, the increased excitation, and the comparably weakly increased inhibition.

Fig. S4. Fig. S4 illustrates that spiking activity during intermittent high frequency oscillations can reflect underlying network structures. In Fig. S4 *A* and *B*, only the recurrent connections of a subpopulation of the excitatory neurons allow supralinear dendritic interactions. The phases of spontaneously increased activity with high-frequency oscillations are essentially restricted to this subpopulation and to the inhibitory population. Fig. S4*A* displays the rate of the inhibitory population (*Upper*, bin size 1 ms) and the spiking activity of 50 inhibitory neurons (*Lower*). Fig. S4*B* displays the rate of the excitatory population (*Upper*, bin size 1 ms) and the spiking activity of 400 excitatory neurons (*Lower*), where neurons 1–200 belong to the subpopulation with supralinear dendritic interactions, and neurons 201–400 belong to the purely conventionally coupled subpopulation. Fig. 3*B* shows the event at $t = 1{,}700$ ms.

Fig. S4 *C–F* displays the spiking dynamics of a network with a feed-forward structure. It consists of a sequence of groups in which connections from one group to the next allow supralinear dendritic interactions (group size: 350 neurons). The spiking activity during phases of high-frequency oscillations reflects this structure. Around times $t_0 = 500$ ms, $t_0 = 1{,}000$ ms, and $t_0 = 1{,}500$ ms, external stimulation excites 40, 60, and 80 randomly chosen neurons within the first group to spiking (spike times normally distributed around t_0, SD 1 ms). The entire structure already is reflected at an initial pulse size of 60 neurons. Fig. S4*C* illustrates

the spiking activity of the inhibitory population (*Upper*) and of the excitatory population (*Lower*). Fig. S4 *D–F* displays the single events. Upper panels display the rate of the excitatory population (bin size 0.5 ms). Lower panels show the spiking activity. The event at t_0 = 1,000 ms is displayed in Fig. 3*C*.

Fig. S5. During phases of increased activity with high-frequency oscillations, the excitatory and the inhibitory neuron populations generate pulses of synchronous spikes. The pulses of the inhibitory population are delayed with respect to the pulses in the excitatory population (Fig. 3*A*), as observed for sharp wave/ripples (SPW/Rs) in experiments. Fig. S5 shows that even quantitative agreement can be achieved if the model incorporates the response properties of the fast hippocampal interneurons relevant for SPW/Rs and the frequent occurrence of projections from excitatory to inhibitory neurons (8–11). I adapt the parameters of the leaky integrate-and-fire neurons to induce response properties similar to those found in ref. 8.

To quantify the time and phase lags, I determined the average spike rates during an event in 10 trials with a simulated time of 25 s. Events i were initiated by external stimulation every 250 ms and were cut out and aligned with respect to the peak times $t_{0,i}$ of the probability distributions of the stimulating pulses. Fig. S5*A* shows the firing rates of the excitatory (blue; *Upper*) and of the inhibitory (red; *Lower*) neuron population during a single event. $t_{0,i}$ is set to $t_{0,i}$ = 0 ms. Fig. S5*B* displays the mean rate for one of the trials. The blue and red curves display the rates of the excitatory and inhibitory populations, respectively. In agreement with experimental observations (12, 13), the time lags generally are very short (1–2 ms) (8–10), and the phase lag is around 90° for the largest pulses (Fig. S5*E*). I further determined the autocorrelation of the rate of the excitatory population and the cross-correlation of the rate activity of the excitatory and inhibitory neuron populations in each trial (correlations not normalized). Fig. S5*C* displays the averaged autocorrelation (black curve) together with two samples from single trials (gray curves) and the SD of the distribution (error bars at every tenth point). The peak at τ = 0 ms is truncated. The averaged autocorrelation assumes its second maximum at $t_{\max,AC}$ = 4.7 ms. The mean of the leading oscillation frequencies of the individual simulations, as determined by the peaks of the power spectral densities, is 201.3 Hz (SD 0.5 Hz). Fig. S5*D* displays the averaged cross-correlation of the excitatory and inhibitory activity (black curve) together with two samples from single trials (gray curves) and the SD of the distribution (error bars at every tenth point). The averaged cross-correlation assumes its first maximum at $t_{\max,CC}$ = 1.2 ms, in agreement with experimental findings (12, 13).

In biological neural networks, additional anatomical and dynamic features could promote synchronous and early firing of inhibitory neurons. Inhibitory neurons are coupled via electrical synapses that promote synchronous firing (14, 15). The excitatory population strongly projects on the inhibitory population (16), and the number of relevant interneurons is comparably small (estimates yield about 5,000–10,000 neurons distributed over CA1) (11, 17). During events these interneurons fire at very high rate, often around 150–250 Hz (12, 13, 18). This data might indicate that the response to excitatory input is saturated: Upon the strong excitatory input during SPW/Rs, and supported by electrical coupling, a majority of interneurons could send a spike before the excitatory input has reached its maximum. Because of refractoriness and recurrent inhibition, subsequent firing of interneurons could be suppressed, and the rate of the interneuron population might decrease although the excitatory input still increases. The comparably broad temporal extent of excitatory pulses in hippocampal SPW/Rs and the resulting broad rising input flanks might strengthen such an effect. The peak of interneuron firing thus could be arbitrarily close to the peak of excitatory firing or even precede it.

In the simulations, the time constants of the excitatory input current and of the membrane in the inhibitory leaky integrate-and-fire model neurons are chosen to generate a 20–80% rise time of 0.6 ms and a half width of 4.0 ms for an excitatory postsynaptic potential (EPSP) of 2.1 mV (8). Further, a 25% probability for the existence of an excitatory-to-inhibitory coupling is assumed (11). The network dimensions and the synaptic delay are at their standard values; the conduction velocity is increased to 350 μm/ms, yielding a mean delay of 1.0 ms between the presynaptic spike and the onset of postsynaptic EPSC (details are given in *SI Text*, *Section C*). These response times are slightly slower than the mean values measured in ref. 8. To align and to gather events in a simple manner, I studied the lags in events initiated by external stimuli. The frequency of external Poissonian input spike trains was decreased for excitatory neurons and increased for inhibitory neurons, suppressing spontaneous events that might interfere with induced ones. Further, higher input rates decrease the effective membrane time constant of neurons (19). Events were initiated by exciting a population of n = 40 neurons to spike. The spike times were chosen randomly according to a Gaussian distribution with SD σ = 1 ms. The mean rate during events was determined in bins of 0.02 ms and thereafter was smoothed using a Gaussian kernel of width σ = 0.25 ms. The phase lag was derived by taking the quotient of the temporal distance between the peak of the excitatory rate and the subsequent peak of the inhibitory rate divided by the temporal distance between subsequent peaks of the rate of the excitatory population.

Fig. S6. In vivo studies in hippocampal region CA3 found that oscillations associated with sharp waves are slower and less pronounced than those in region CA1 (12, 20). This decrease of oscillation frequency might be due to the prominent long-range, global connectivity in CA3 (17, 21–24) and the strongly inhomogeneous conduction velocity. Fig. S6 illustrates the idea.

Comparably little is known about the nonlinear properties of dendrites in CA3, but the high similarity between CA1 and CA3 neurons suggests properties similar to those in CA1 (17). I thus simulated a network incorporating supralinear dendritic interactions as for the CA1 model. The network is spread over a square with edge length X = 2.8 mm (mean distance between neurons, 1.45 mm) (22–24) and has a Gaussian conduction velocity distribution with a mean of 390 μm/ms and a SD of 140 μm/ms (ref. 25; values in ref. 26 are smaller), truncated at zero. The network shows spontaneously intermittent events of increased activity. There are only weak (if any) oscillations in the rate activity during single events, as illustrated by Fig. S6*A*. The inhibitory population does not show oscillations because of the strong dispersion of inputs from the excitatory population. Their occurrence might require local coupling of interneurons or more pronounced oscillations of the excitatory population. The global power spectral density of the spike rates of excitatory neurons (squared amplitude of the discrete modes divided by the bandwidth) is displayed in Fig. S6*B* for 50 s of simulated time (Hamming window function, power spectrum smoothed with Gaussian kernel of width σ = 11 Hz). It has a weak peak originating from oscillations associated with events and from oscillations during background activity (20). The leading frequency is about 140 Hz, compatible with the frequency range observed in CA3 in vivo experiments (12, 20).

For comparison, in Fig. S6 *C* and *D*, the edge length was reduced to X = 450 μm (i.e., to the typical slice thickness in an in vitro experiment) (27–29). The network shows spontaneously intermittent events of increased activity with pronounced, highly synchronous rate oscillations in both neuron populations at a leading oscillation frequency of 198 Hz, in agreement with in vitro observations (27–29). Fig. S6*C* shows two instances of the rate activity of the excitatory population during events. The in-

cidence of events was higher in the simulation with reduced edge length. To allow a direct comparison of the spectral power in both simulations, the number of events was reduced to the number in the simulation with large X by cutting out (deleting) random events. The power spectrum (Fig. S6*D*) shows a considerably larger peak at the leading frequency compared with the spectrum of the network with large X. This larger peak reflects the more pronounced oscillations during events. (For the original rate activity in the network with reduced X, the peak in Fig. S6*D* is about twice as high, reaching 21 spikes^2/ms.)

SI Section B: Further Analysis of the Model Dynamics

Estimates of the Frequency Range. In the following subsections, I estimate the range of the frequencies predicted by my models. Action potentials in CA1 which are generated by dendritic spikes have been found to occur 5 ms after presynaptic stimulation with submillisecond temporal precision (5). We therefore expect the peaks of maximally synchronized activity to be separated by time intervals of about 5 ms, i.e., an oscillation frequency of about 200 Hz. The frequency is remarkably stable even when the model parameters are varied over broad ranges. This stability reflects the high temporal precision and the fixed time scale introduced by fast dendritic spikes in the neuronal output (5, 7, 30). The analytical and numerical predictions of models 1 and 2, in particular the dependencies on the model parameters, agree very well. I further derived analytical estimates in a low-frequency limit which yield lower frequency bounds, with similar dependencies on the parameters. The results are similar because the mechanism underlying the generation of high-frequency oscillations is the same in each of the models—namely, the propagation of synchrony mediated by supralinear dendritic interactions.

The oscillation frequency ranges are in very good agreement with the experimentally observed range of 140–250 Hz (12, 27–29, 31, 32) for high-frequency ripples. The ranges depend mainly on the delay times of the excitatory to excitatory connections, i.e., on the axonal delay time, the synaptic delay, and the latency of the dendritic spike.

Analytical Estimates of the Frequency Range. In model 1, the temporal difference τ between presynaptic spiking and postsynaptic spiking evoked by a dendritic spike is constant. τ can be decomposed into two contributions,

$$\tau = \tau_{\mathrm{Ax}} + \tau_{\mathrm{post,AP}}, \qquad \text{[S1]}$$

(*i*) the axonal delay τ_{Ax}, i.e., the time from the onset of the presynaptic action potential to the onset of the synaptic transmission, and (*ii*) the time $\tau_{\mathrm{post,AP}}$ from the onset of synaptic transmission to the onset of the postsynaptic action potential. The range of local axonal interconnections in CA1 has been estimated to be of the order of 300 μm (33, 34); in some directions, connections were found extending over 400 μm and more (33–36). In my modeling approach I therefore assume that the networks of neurons cover a square patch of tissue with side length X, where X is 200–500 μm, and the mean spatial distance $\bar{d}_X$ between two neurons is 100–260 μm (*SI Text*, *Section C*). Networks with larger X might serve as models for different regions (main text and Fig. S6). I assume that the apparent conduction velocity of action potentials v_{Ax} for the thin, unmyelinated local connections in CA1 is in the lower range of velocities measured in unmyelinated axons of the hippocampus, i.e., 200–400 μm/ms (25, 26). The network is randomly connected: Connections are present with constant probabilities, which depend on the type of the presynaptic and the postsynaptic neurons. τ_{Ax} is computed as the mean distance divided by the apparent conduction velocity and is in the range of 0.3–1.3 ms. $\tau_{\mathrm{post,AP}}$ can be estimated from the time $\tau_{\mathrm{stim,AP}}$ between focal synaptic stimulation and the peak of the postsynaptic action potential by subtracting a time τ_{stim} for stimulation and for the rise τ_{rise} of the action potential. In the presence of dendritic spikes, the timing of postsynaptic action potentials is remarkably precise. Mean values of $\tau_{\mathrm{stim,AP}}$ are 5–5.1 ms (depending on the stimulus protocol); the SD of the distributions and the temporal jitters between trials are about 0.1 ms (5). Focal synaptic stimulation generally is very fast. I assume τ_{stim} to lie between 0 and 0.2 ms; the precise value depends on experimental conditions such as the position of the presynaptic axon and the synaptic terminal relative to the electrode. Typical values for the rise time of an action potential in hippocampal region CA1 under in vitro experimental conditions are 0.3–0.5 ms (5, 37, 38), yielding a range of 4.3–4.8 ms for the values of $\tau_{\mathrm{post,AP}}$.

Taken together, the estimations for $\tau = \tau_{\mathrm{Ax}} + \tau_{\mathrm{post,AP}}$ yield a range of 4.6–6.1 ms and thus a frequency range for the oscillation frequency $1/\tau$ of 164–220 Hz, in very good agreement with the typical range of 140–250 Hz (12, 32, 27–29, 31) found for high-frequency ripple oscillations in in vivo and in vitro neurobiological experiments. Oscillation frequencies outside the range of the estimation, such as 240 Hz or 250 Hz reported in refs. 29 and 28, might be caused by the specific experimental conditions, the animal species studied, or the influence of different mechanisms (39). Systematic errors arising from sparse data (e.g., about the axonal range in CA1 or the connection probability) might have distorted the estimation of frequency range. However, even if one assumes considerably larger errors of the components of τ, the results still agree well with the experimentally determined frequencies of SPW/Rs in the hippocampus. In the simulations, I used values near the middle of the biologically plausible ranges, avoiding extremes. If not stated otherwise, for model 1, I used $\tau = 5$ ms.

I now connect the parameters of model 1 with those of model 2 to allow a comparison of the predicted oscillation frequencies. In model 2, the parameters X and v_{Ax} characterize the inhomogeneous axonal delay distribution. These parameters are connected to the model 1 parameter τ_{Ax} by $\tau_{\mathrm{Ax}} = \bar{d}_X / v_{\mathrm{Ax}}$. The contribution $\tau_{\mathrm{post,AP}}$ is in model 2 determined (*i*) by the time τ_{ExEx} between the onset of synaptic transmission and the onset of the somatic AMPA response, (*ii*) by the latency τ_{DS} from the AMPA onset to the onset of the somatic response to the dendritic spike, and (*iii*) by the time $t_{\mathrm{DS,AP}}$ between the onset of the response to a dendritic spike and the onset of the postsynaptic action potential,

$$\tau_{\mathrm{post,AP}} = \tau_{\mathrm{ExEx}} + \tau_{\mathrm{DS}} + t_{\mathrm{DS,AP}}. \qquad \text{[S2]}$$

The third contribution is variable, because the membrane potential response to a dendritic spike has a finite rise time, and the action potentials are generated during the rise of the membrane potential in response to a dendritic spike. Because the rise is steep and the peak is sharp, I set $t_{\mathrm{DS,AP}} = \tau_{\mathrm{rise,DS}}$ when computing $\tau_{\mathrm{post,AP}}$ for model 1. Here, $\tau_{\mathrm{rise,DS}}$ is the time between the onset of the response to a dendritic spike and the peak in model 2. $\tau_{\mathrm{rise,DS}}$ is determined by the current from the dendritic spike. It depends slightly on τ_{DS} and takes values of about 0.9 ms.

Fig. S7 shows the dependence of the oscillation frequency $1/\tau$ in model 1 on X, τ_{ExEx}, and τ_{DS}. If not varied, the values of the parameters are $X = 350$ μm ($v_{\mathrm{Ax}} = 300$ μm/ms), $\tau_{\mathrm{ExEx}} = 1$ ms, $\tau_{\mathrm{DS}} = 2.7$ ms, and $\tau_{\mathrm{rise,DS}} = 0.9$ ms, in agreement with experimental data (5, 40–42). Fig. S7 shows that the frequency decreases with increasing X, predicting that a network with reduced extent (e.g., because of slice preparation) generates higher oscillation frequencies. Additive changes in τ_{ExEx} are equivalent to additive changes in $\tau_{\mathrm{post,AP}}$. The same holds for additive changes in τ_{DS} because $t_{\mathrm{DS,AP}}$ is taken as a constant. The results in the first paragraph in this subsection and the assumed standard parameter values yield biologically plausible ranges of 0.7–1.2 ms for τ_{ExEx} and 2.4–2.9 ms for τ_{DS}, indicated by gray dashed lines in Fig. S7 *B* and *C*. These ranges are equivalent to the range of 4.3–4.8 ms

estimated for $\tau_{post,AP}$. The frequencies generated by networks with parameters in considerably larger ranges, e.g., a range of 0.5–1.5 ms for τ_{ExEx} (40–42), still would agree with experimentally determined frequencies of ripple oscillations.

I further derived an analytical estimate for the oscillation frequency which accounts for the finite interaction window and temporally extended pulses. I computed the temporal difference τ between the peaks of an extended initial pulse and the response pulse. In Poissonian approximation and in the limit of small-input spike frequency, the response pulse and thus an equation for τ can be explicitly derived. The oscillation frequency, approximated by $1/\tau$, can be computed by solving this equation numerically (blue curves in Figs. S7–S9). An upper estimate can be derived analytically, whose inverse yields a lower estimate for the oscillation frequency (gray curves in Figs. S7–S9).

Numerical Estimates of the Frequency Range. Model 2 generates irregular activity and spontaneous phases of enhanced activity with high-frequency oscillations. In the following subsection, I show that the spontaneous generation of events and the frequency range are robust against changes of network parameters. The parameter dependencies are very similar to those in model 1. (*i*) I first consider the dependence on parameters that influence the oscillation frequency in model 1, namely the edge length X of the square covered by the network, the synaptic delay τ_{ExEx} of couplings from excitatory neurons to excitatory neurons, and the latency τ_{DS} from the AMPA onset to the onset of the somatic response to the dendritic spike (Fig. S7). (*ii*) I then study the dependence on other timescales that might influence the oscillation frequency in model 2, such as the window for supralinear interaction Δt and the synaptic and postsynaptic delay τ_{ExIn} of inhibitory neuron to excitatory neuron synapses (Fig. S8). The latter determines the times at which the inhibitory feedback reaches the excitatory neurons and would have a strong influence if feedback inhibition was important for oscillation frequency. Equivalently, I could have considered τ_{InEx}. (*iii*) Finally, I investigate the dependence on nontemporal parameters that might influence the oscillation frequency by means of the coupling strengths within the network (Fig. S9). I examine the dependence on the recurrent coupling strengths between excitatory neurons (changed by a factor c_{EE}), on the strengths of all internal and external excitatory couplings (changed by a factor c_E), and on the strengths of all internal and external inhibitory couplings (changed by a factor c_I). For each set of parameters, six simulations were run with randomly chosen networks and random initial conditions, each for 20 s of simulated time. The resulting spike trains were gathered for the excitatory and inhibitory population separately, and the instantaneous rates were derived in 0.5-ms bins. The leading frequency in the range 120–700 Hz was determined by the global maximum of the discrete power spectrum of the rate (Hamming windowing function; the power spectrum was smoothed using a Gaussian kernel with width $\sigma = 11$ Hz).

The dependence of the oscillation frequency on the parameters X, τ_{ExEx}, and τ_{DS} is displayed in Fig. S7. Model 1, model 2, and the estimation in the low-frequency limit show the same functional dependence on the parameters. In the numerical simulations, X was varied from 100–1,000 μm in steps of 30 μm; frequencies corresponding to larger values of X, exceeding the estimated range for CA1, might be characteristic for high-frequency oscillations in different areas. τ_{ExEx} was varied from 0.4–1.6 ms in steps of 0.05 ms. τ_{DS} was varied from 2–3.5 ms in steps of 0.05 ms. (If not varied, the parameters are at their standard values.) The dynamics of model 2 is robust against changes in X, τ_{ExEx}, and τ_{DS} for the entire range considered.

Fig. S8 displays the dependence of the oscillation frequency on the parameters Δt and τ_{ExIn}. The frequency prediction of model 1 is independent of these parameters, which do not occur in the model. The prediction in the low-frequency approximation depends on Δt. As Δt increases, the longer sampling time available around the peak of the input pulse shifts the peak of the generated dendritic spikes to later times. The temporal distance between the initial pulse and the response pulse increases, and the frequency decreases. The prediction does not depend on the parameter τ_{ExIn}. In model 2, both parameters could, in principle, influence the oscillation frequency. However, upon changes of Δt within the experimentally determined range for reliable amplification, the oscillation frequency remains essentially invariant. Here, effects such as reaching the threshold for dendritic spiking earlier with increased Δt and the induction of earlier successive pulses by larger pulses might balance effects such as the induction of later pulse peaks by longer sampling times. For very small Δt, no events are generated, because there are not enough spike arrivals within the window to generate dendritic spikes. With increasing Δt, the incidence and size of events increases. For larger Δt, the underlying dynamics becomes pathological, consisting of an uninterrupted series of large events, and the leading frequency increases. This change in dynamics can be partially prevented by adjusting the other network parameters. The range depicted by gray dashed lines in Fig. S8*A* is the range found for interaction windows that give rise to reliable supralinear interaction when the input strengths are not too large. Windows for very strong inputs or unreliable amplification can be larger (5). The indirect influence of τ_{ExIn} on the oscillation frequency is weak within the biological range of about 0.3–1.5 ms (10, 43, 44). The dynamics are highly robust against changes in this parameter. Δt was varied from 1.6–3.8 ms in steps of 0.1 ms. τ_{ExIn} was varied from 0 to 1.6 ms in steps of 0.1 ms.

Fig. S9 shows the dependence of the oscillation frequency on the coupling strengths. The strengths of recurrent couplings between excitatory neurons (factor c_{ExEx}) (Fig. S9 *A* and *D*), of all excitatory couplings (factor c_{Ex}) (Fig. S9 *B* and *E*), and of all inhibitory couplings (factor c_{In}) (Fig. S9 *C* and *F*) were varied relative to the standard values (*SI Section C*). The networks generate three types of activity: low-frequency irregular activity without events, low-frequency irregular activity with events, and continual high-frequency activity. Low-frequency irregular activity without events does not have a pronounced leading frequency within the range of 120–700 Hz. Continual high-frequency activity is characterized by leading frequencies higher than 200 Hz. The high-frequency state was detected by checking whether the mean frequency of each excitatory neuron was higher than 100 Hz for at least 100 ms. The trial was stopped after the condition was met, because this state is of minor interest for the present study, and the entire trial was analyzed. Because the trial was broken off quickly after the transition, the highest frequency peak detected sometimes is the peak around 200 Hz from the transient. If the state was realized even before the usual network equilibration time was reached, the last 50 ms were analyzed.

Model 2 shows robust occurrence of low-frequency irregular activity with events. Fig. S9 displays the range in which low-frequency irregular activity with events reliably occurs between the blue and red dashed lines. Beyond the blue dashed line, at least one of the trials did not show any event; beyond the red dashed line, at least one of the trials underwent a transition to the state of continual high-frequency firing. The coupling strengths do not influence the oscillation frequencies in model 1 (green straight lines, shown for the range in which the events in model 2 occurred reliably) or in the low-frequency limit (blue and gray straight lines). The range of c_{ExEx} that gives rise to this dynamics covers nearly the entire range where four inputs generate a dendritic spike. (See Fig. S2 for similar results in model 1.) For increased excitatory couplings and reduced inhibitory couplings, there is an increase of event size, incidence, and also oscillation frequency (probably because of indirect effects such as a decrease in interpulse interval with an increase in pulse size). Fig. S9 shows a stronger effect upon changes in inhibitory coupling (Fig. S9 *C* and *F*), highlighting the role of inhibition in shaping

the events. Near the border to continual high-frequency firing, the activity consists of markedly increased events.

Changes of the order of 10% in the c factors entail large differences in the total coupling strength in the network and thus have a strong impact on the network dynamics. The activity is robust against such changes, although features such as neural adaptation and short-term synaptic plasticity that stabilize the network frequency and could support the emergence of intermittent events in biological neural networks are not incorporated in the model (e.g., refs. 37 and 45). c_{ExEx} was varied from 0.9–1.3, c_{Ex} was varied from 0.85–1.2, and c_{In} was varied from 0.8–1.15, each factor in steps of 0.01.

A Model for Epilepsy? The results described in the previous subsection suggest two possible models for transitions to glutamate-dependent epileptic activity. If inhibition is sufficiently strong and excitation sufficiently weak, model 2-type networks show uninterrupted irregular activity. Upon decrease of inhibition or increase of excitation, they start to generate events. This dynamics might model a transition from a healthy ground state to a state with intermittent pathological high-frequency oscillations. The network models can be extended to study the influence of single-neuron dynamics such as (pathological) bursting. Events can be localized to subnetworks (Fig. 3*B*), suggesting an application to epileptic foci. Multiple foci that are out of phase might lead to very high-frequency oscillations, as suggested in ref. 39.

Further, we can consider the state in which intermittent events are generated as the healthy state. Upon decrease of inhibition or increase of excitation, the events increase in size, the activity approaches a nearly uninterrupted series of events, and the oscillation frequency increases. This transition might explain transitions from healthy intermittent high-frequency oscillations to epileptiform events. A transition to intermittent epileptiform events as found in slices of hippocampal region CA3 (27) might arise when properties such as short-term synaptic plasticity, bursting, and neural adaptation are incorporated in the network model.

SI Section C: Details of Models 1 and 2

Model 1. In model 1, the subthreshold dynamics of the membrane potential V_l of neuron $l \in \{1, \ldots, N\}$ is determined by

$$\frac{dV_l(t)}{dt} = -\gamma_l V_l(t) + \sum_f \left[\sigma\left(\sum_{j\in M_{\mathrm{Ex},l}(f)} \varepsilon_{lj}\right) + \sum_{j\in M_{\mathrm{In},l}(f)} \varepsilon_{lj}\right]\delta(t - t^f - \tau) + I_{0,l}, \qquad [S3]$$

where t^f denotes the firing times in the network, $\gamma_l = 1/\tau_{\mathrm{mem},l}$ is the inverse membrane time constant, $I_{0,l}$ denotes the constant input current, τ denotes the coupling delay, $\delta(.)$ is the Dirac δ-distribution, and ε_{lj} denotes the coupling strength from neuron j to neuron l. The sets of indices of neurons sending at time t^f excitatory and inhibitory inputs to neuron l are denoted by $M_{\mathrm{Ex},l}(f)$ and $M_{\mathrm{In},l}(f)$, respectively. When the neuron reaches or exceeds the threshold Θ_l, it sends a spike and is reset to $V_{\mathrm{r},l}$.

Due to the infinitesimal rise time, the peak excitatory postsynaptic potential (EPSP) generated by an excitatory input is reached at the time of input arrival and equals the size of the jump height if all other inputs are absent. σ thus maps the peak EPSP expected by linear summation of the simultaneous inputs to the actual peak EPSP, which can be read off or straightforwardly deduced from experimental literature (5, 6, 46). I set $\sigma(\varepsilon) = \varepsilon$ if $\varepsilon \le V_a$, and $\sigma(\varepsilon) = V_c$ if $\varepsilon > V_a$ with $V_a = 3.8$ mV and $V_c = 10$ mV (5).

Other network parameters are $N = 1{,}000$, $p_0 = 0.3$, $p_{\mathrm{Ex}} = p_{\mathrm{In}} = 0.5$, $\tau_{\mathrm{mem},l} = 14$ ms $= 1/\gamma_l$, $\tau = 5$ ms, $I_{0,l}\tau_{\mathrm{mem},l} = 17.8$ mV, $\Theta_l = 15$ mV, $V_{\mathrm{r},l} = 0$ mV. If not stated otherwise, coupling strengths are $\varepsilon_{lj} = 0.35$ mV for an excitatory coupling and $\varepsilon_{lj} = -0.35$ mV for an inhibitory coupling; the onset of supralinear amplification thus is at 11 excitatory inputs.

Model 2. In model 2, the subthreshold dynamics of the membrane potential V_l of neuron l is determined by

$$C_{m,l}\frac{dV_l(t)}{dt} = g_{L,l}(V_{\mathrm{rest},l} - V_l(t)) + g_{A,l}(t)(E_{\mathrm{Ex}} - V_l(t)) + g_{G,l}(t)(E_{\mathrm{In}} - V_l(t)) + I_{\mathrm{DS},l}(t), \qquad [S4]$$

where $C_{m,l}$ is the membrane capacity of the neuron, $g_{L,l}$ is the resting conductance, $V_{\mathrm{rest},l}$ is the resting potential, E_{Ex} and E_{In} are the reversal potentials, and $g_{A,l}(t)$ and $g_{G,l}(t)$ are the conductances of AMPA and $\mathrm{GABA_A}$ synaptic populations, respectively. $I_{\mathrm{DS},l}(t)$ models the current pulses caused by dendritic spikes. In $g_{A,l}(t)$ and $g_{G,l}(t)$, the time course of synaptic conductances caused by single inputs is given by the difference between two exponential functions (47). Time constants are $\tau_{A,1}$ and $\tau_{G,1}$ for the exponential function dominating the decay and $\tau_{A,2}$ and $\tau_{G,2}$ for the exponential function dominating the rise of the conductance. The peak conductance (coupling strength) for a coupling from neuron j to neuron l is $g_{\mathrm{max},lj}$. When the membrane potential reaches the spike threshold Θ_l, the neuron sends a spike to its postsynaptic neurons and is reset to $V_{r,l}$. For dendritic spike generation, the sum $g_{\Delta t}$ of excitatory input strengths (characterized by the coupling strengths) arriving at an excitatory neuron l within the time window Δt is considered and compared with a threshold g_Θ. For standard parameters, four inputs within Δt initiate the generation of a dendritic spike. At a time τ_{DS} after this initiation, a current pulse is generated in the soma. This current pulse is modeled as the sum of three exponential functions,

$$I_{\mathrm{DS},l}(t) = c(g_{\Delta t})\left[-A\exp\left(-\frac{t}{\tau_{\mathrm{DS},1}}\right) + B\exp\left(-\frac{t}{\tau_{\mathrm{DS},2}}\right) - C\exp\left(-\frac{t}{\tau_{\mathrm{DS},3}}\right)\right], \qquad [S5]$$

with prefactors $-A$, B, $-C$, decay time constants $\tau_{\mathrm{DS},1}$, $\tau_{\mathrm{DS},2}$, $\tau_{\mathrm{DS},3}$, and a dimensionless correction factor $c(g_{\Delta t})$. The correction factor modulates the pulse strength, ensuring that σ reaches the experimentally observed region of saturation. At very high excitatory inputs, the conventionally generated depolarization exceeds the level of saturation, and σ increases.

In simulations, the number of neurons used usually is $N = 1{,}000$; for the structured networks it is augmented by 500 excitatory neurons. The size of the subpopulation incorporating supralinear dendritic interactions in Fig. 3*B* and Fig. S4 *A* and *B* is 900 neurons. Directed couplings from excitatory to excitatory, from excitatory to inhibitory, from inhibitory to excitatory, and from inhibitory to inhibitory neurons are present independently, with probabilities p_{ExEx}, p_{InEx}, p_{ExIn}, and p_{InIn}, respectively. Of particular interest for the model is p_{ExEx}. The recurrent excitatory connectivity in CA1 is sparse but significant. A connection probability of 1% was estimated in a distance of 200 μm (37). Anatomical studies, which found a local axonal plexus besides long-range axonal branches (33, 34), and a comparison with neocortex (48) suggest that it increases with proximity. I assume that in CA1 networks local coupling dominates the generation of ripple oscillations, whereas in native CA3 networks (Fig. S6) the influence of global connectivity is more important (17, 21–24). Large numbers of neurons coherently participating in SPW/Rs (49), electrical synapses between pyramidal neurons (50, 51), nonrandom network connectivity patterns (37), external inputs to basal dendrites (17), and $\mathrm{GABA_A}$-mediated excitation (28) also might compensate for sparse coupling. I choose a sparse connectivity of $p_{\mathrm{ExEx}} = 0.08$ for the comparably small, purely random networks considered. If not stated otherwise (see the section Structured Networks in the main text), recurrent excitatory inputs

to the same neuron can interact nonlinearly; i.e., they are assumed to arrive at the same dendrite or dendritic compartment.

The axonal delays account for the length of local collaterals and for the spatial spread of a network of about 1,000 neurons in CA1: The distances between neurons are drawn independently according to the probability distribution for the distance of two neurons on an area of 350 μm × 350 μm (17, 24, 52), and the delays are computed assuming a spike propagation velocity of 300 μm/ms (25, 26).

The parameters of single neurons are $C_{m,l}$ = 400 pF, $g_{L,l}$ = 25 nS, $V_{\mathrm{rest},l} = V_{r,l}$ = −65 mV, E_{Ex} = 0 mV, E_{In} = −75 mV, Θ_l = −45 mV, refractory period t_{ref} = 3 ms (17, 38) for the excitatory population, and $C_{m,l}$ = 200 pF, $g_{L,l}$ = 25 nS, $V_{\mathrm{rest},l} = V_{r,l}$ = −65 mV, E_{Ex} = 0 mV, E_{In} = −75 mV, Θ_l = −55 mV, t_{ref} = 2 ms (8, 53) for the inhibitory population. The parameters for couplings from excitatory-to-excitatory neurons are p_{ExEx} = 0.08 (refs. 17, 37, and 40 and comments above), τ_{ExEx} = 1 ms (delay without axonal delay; *SI Text*, *Section B*) (40–42), $g_{\mathrm{max},l,j}$ = 2.3 nS (37, 40), $\tau_{A,1}$ = 2.5 ms, $\tau_{A,2}$ = 0.5 ms (54, 55); further, Δt = 2 ms (5–7), g_Θ = 8.65 nS (corresponding to the conductance generating a single EPSP of about 3.8 mV (5)), τ_{DS} = 2.7 ms (*SI Text*, *Section B*), A = 55 nA, B = 64 nA, C = 9 nA, $\tau_{\mathrm{DS},1}$ = 0.2 ms, $\tau_{\mathrm{DS},2}$ = 0.3 ms, $\tau_{\mathrm{DS},3}$ = 0.7 ms, $c(g)$ = max(1.46–0.053 g/nS, 0) and the refractory period of the dendrite, $t_{\mathrm{ref},D} = \tau_{\mathrm{DS}} + 2.5$ ms (estimated generation time of the dendritic spike plus refractory period t_{ref}; no dendritic spikes are generated within this period). For excitatory-to-inhibitory couplings, the parameters are p_{InEx} = 0.1 (11), τ_{InEx} = 0.5 ms, $g_{\mathrm{max},l,j}$ = 3.2 nS, $\tau_{A,1}$ = 2 ms, $\tau_{A,2}$ = 0.35 ms (8, 16, 56); for inhibitory-to-excitatory couplings, p_{ExIn} = 0.1 (11), τ_{ExIn} = 1 ms (43, 44), $g_{\mathrm{max},l,j}$ = 5 nS (43, 44, 57), $\tau_{G,1}$ = 4 ms (44, 58), $\tau_{G,2}$ = 0.3 ms (44, 57); and for inhibitory-to-inhibitory couplings, p_{InIn} = 0.02 (11), τ_{InIn} = 0.5 ms (44, 59), $g_{\mathrm{max},l,j}$ = 4 nS, $\tau_{G,1}$ = 2.5 ms, $\tau_{G,2}$ = 0.4 ms. Some of these parameters, such as p_{ExIn}, were modified from the experimentally determined values to avoid pathological network dynamics. In leaky integrate-and-fire neurons the parameters do not lead to response properties as fast as found experimentally for interneurons (8). In Fig. S5, I therefore assumed for interneurons $C_{m,l}$ = 100 pF, $g_{L,l}$ = 33 nS. The parameters of excitatory-to-inhibitory synapses are p_{InEx} = 0.25 (11), $g_{\mathrm{max},l,j}$ = 2.85 nS (an input strength of $g_{\mathrm{max},l,j}$ = 4.2 nS generates an EPSP of 2.1 mV from the resting potential), $\tau_{A,1}$ = 0.7 ms, $\tau_{A,2}$ = 0.25 ms. The strengths of the internal inhibitory-to-excitatory synapses are $g_{\mathrm{max},l,j}$ = 4 nS. Further, t_{ref} = 2.5 ms was assumed for inhibitory neurons, this value reduces multiple firing upon a single pulse from the excitatory population (an increased strength of inhibitory-to-inhibitory projections has a similar effect). The spike propagation velocity was assumed to be 350 μm/ms; the remaining parameters are as before.

Neurons receive external Poisson spike trains with a rate of 2.3 kHz (excitatory neurons) and a rate of 0.5 kHz (inhibitory neurons), each with a ratio of 75% excitatory and 25% inhibitory inputs. In Fig. S5, the input rates were 2.2 kHz (excitatory neurons) and 2.2 kHz (inhibitory neurons). In Fig. S6, the input rates were 2.9 kHz (excitatory neurons) and 0.7 kHz (inhibitory neurons). If not stated otherwise, the strengths of the external inputs equal the strengths of the internal inputs, but external inputs do not contribute to the generation of dendritic spikes.

1. Diesmann M, Gewaltig MO, Aertsen A (1999) Stable propagation of synchronous spiking in cortical neural networks. *Nature* 402:529–533.
2. Vogels T, Abbott L (2005) Signal propagation and logic gating in networks of integrate-and-fire neurons. *J Neurosci* 25:10786–10795.
3. Kumar A, Rotter S, Aertsen A (2008) Conditions for propagating synchronous spiking and asynchronous firing rates in a cortical network model. *J Neurosci* 28: 5268–5280.
4. Abeles M, Hayon G, Lehmann D (2004) Modeling compositionality by dynamic binding of synfire chains. *J Comput Neurosci* 17:179–201.
5. Ariav G, Polsky A, Schiller J (2003) Submillisecond precision of the input-output transformation function mediated by fast sodium dendritic spikes in basal dendrites of CA1 pyramidal neurons. *J Neurosci* 23:7750–7758.
6. Gasparini S, Migliore M, Magee J (2004) On the initiation and propagation of dendritic spikes in CA1 pyramidal neurons. *J Neurosci* 24:11046–11056.
7. Gasparini S, Magee J (2006) State-dependent dendritic computation in hippocampal CA1 pyramidal neurons. *J Neurosci* 26:2088–2100.
8. Geiger J, Lübke J, Roth A, Frotschner M, Jonas P (1997) Submillisecond AMPA receptor signaling at a principal neuron-interneuron synapse. *Neuron* 18:1009–1023.
9. Csicsvari J, Hirase H, Czurko A, Buzsáki G (1998) Reliability and state dependence of pyramidal cell-interneuron synapses in the hippocampus: An ensemble approach in the behaving rat. *Neuron* 21:179–189.
10. Jonas P, Bischofberger J, Fricker D, Miles R (2004) Interneuron diversity series: Fast in, fast out: Temporal and spatial signal processing in hippocampal interneurons. *Trends Neurosci* 27:30–40.
11. Ascoli G, Atkeson J (2005) Incorporating anatomically realistic cellular-level connectivity in neural network models of the rat hippocampus. *Biosystems* 79: 173–181.
12. Ylinen A, et al. (1995) Sharp wave-associated high-frequency oscillation (200 Hz) in the intact hippocampus: Network and intracellular mechanisms. *J Neurosci* 15: 30–46.
13. Csicsvari J, Hirase H, Czurkó A, Mamiya A, Buzsáki G (1999) Oscillatory coupling of hippocampal pyramidal cells and interneurons in the behaving rat. *J Neurosci* 19: 274–287.
14. Fukuda T, Kosaka T (2000) Gap junctions linking the dendritic network of GABAergic interneurons in the hippocampus. *J Neurosci* 20:1519–1528.
15. Galarreta M, Hestrin S (2001) Electrical synapses between GABA-releasing interneurons. *Nat Rev Neurosci* 2:425–433.
16. Galarreta M, Hestrin S (2001) Spike transmission and synchrony detection in networks of GABAergic interneurons. *Science* 292:2295–2299.
17. Andersen P, Morris R, Amaral D, Bliss T, O'Keefe J (2007) *The Hippocampus Book* (Oxford Univ Press, Oxford, UK).
18. Klausberger T, et al. (2003) Brain-state- and cell-type-specific firing of hippocampal interneurons in vivo. *Nature* 421:844–848.
19. Kumar A, Schrader S, Aertsen A, Rotter S (2008) The high-conductance state of cortical networks. *Neural Comput* 20:1–34.
20. Csicsvari J, Hirase H, Czurkó A, Mamiya A, Buzsáki G (1999) Fast network oscillations in the hippocampal CA1 region of the behaving rat. *J Neurosci* 19:RC20:1–4.
21. Ishizuka N, Weber J, Amaral D (1990) Organization of intrahippocampal projections originating from CA3 pyramidal cells in the rat. *J Comp Neurol* 295:580–623.
22. Sik A, Tamamaki N, Freund T (1993) Complete axon arborization of a single CA3 pyramidal cell in the rat hippocampus. *Eur J Neurosci* 5:1719–1728.
23. Li X, Somogyi P, Ylinen A, Buzsáki G (1994) The hippocampal ca3 network: An in vivo intracellular labeling study. *J Comp Neurol* 339:181–208.
24. Ishizuka N, Cowan W, Amaral D (1995) A quantitative analysis of the dendritic organization of pyramidal cells in the rat hippocampus. *J Comp Neurol* 362:17–45.
25. Andersen P, Soleng A, Raastad M (2000) The hippocampal lamellar hypothesis revisited. *Brain Res* 886:165–171.
26. Meeks J, Mennerick S (2006) Action potential initiation and propagation in CA3 pyramidal axons. *J Neurophysiol* 97:3460–3472.
27. Maier N, Nimmrich V, Draguhn A (2003) Cellular and network mechanisms underlying spontaneous sharp wave-ripple complexes in mouse hippocampal slices. *J Physiol* 550: 873–887.
28. Nimmrich V, Maier N, Schmitz D, Draguhn A (2005) Induced sharp wave-ripple complexes in the absence of synaptic inhibition in mouse hippocampal slices. *J Physiol* 563:663–670.
29. Both M, Bähner F, von Bohlen und Halbach O, Draguhn A (2008) Propagation of specific network patterns through the mouse hippocampus. *Hippocampus* 18: 899–908.
30. Losonczy A, Makara J, Magee J (2008) Compartmentalized dendritic plasticity and input feature storage in neurons. *Nature* 452:436–441.
31. Buzsáki G, Horváth Z, Urioste R, Hetke J, Wise K (1992) High frequency network oscillation in the hippocampus. *Science* 256:1025–1027.
32. Chrobak J, Buzsáki G (1996) High-frequency oscillations in the output network of the hippocampal-entorhinal axis of the freely behaving rat. *J Neurosci* 16:3056–3066.
33. Knowles W, Schwartzkroin P (1981) Axonal ramifications of hippocampal CA1 pyramidal cells. *J Neurosci* 1:1236–1241.
34. Orman R, von Gizycki H, Lytton W, Stewart M (2008) Local axon collaterals of area CA1 support spread of epileptiform discharges within CA1, but propagation is unidirectional. *Hippocampus* 18:1021–1033.
35. Christian E, Dudek F (1988) Electrophysiological evidence from glutamate microapplications for local excitatory circuits in the CA1 area of rat hippocampal slices. *J Neurophysiol* 59:110–123.
36. Oram M, Wiener M, Lestienne R, Richmond B (1999) Stochastic nature of precisely timed spike patterns in visual system neuronal responses. *J Neurophysiol* 81: 3021–3033.
37. Deuchars J, Thomson A (1996) CA1 pyramid-pyramid connections in rat hippocampus *in vitro*: Dual intracellular recordings with biocytin filling. *Neuroscience* 74:1009–1018.
38. Staff N, Jung HY, Thiagarajan T, Yao M, Spruston N (2000) Resting and active properties of pyramidal neurons in subiculum and CA1 of rat hippocampus. *J Neurophysiol* 84:2398–2408.

39. Engel J, Bragin A, Staba R, Mody I (2009) High-frequency oscillations: What is normal and what is not? *Epilepsia* 50:598–604.
40. Miles R, Wong R (1986) Excitatory synaptic interactions between CA3 neurones in the guinea pig hippocampus. *J Physiol* 373:397–418.
41. Debanne D, Guérineau N, Gähwiler B, Thompson S (1995) Physiology and pharmacology of unitary synaptic connections between pairs of cells in areas CA3 and CA1 of rat hippocampal slice cultures. *J Neurophysiol* 73:1282–1294.
42. Boudkkazi S, et al. (2007) Release-dependent variations in synaptic latency: A putative code for short- and long-term synaptic dynamics. *Neuron* 56:1048–1060.
43. Kraushaar U, Jonas P (2000) Efficacy and stability of quantal GABA release at a hippocampal interneuron-principal neuron synapse. *J Neurosci* 20:5594–5607.
44. Bartos M, et al. (2002) Fast synaptic inhibition promotes synchronized gamma oscillations in hippocampal interneuron networks. *Proc Natl Acad Sci USA* 99:13222–13227.
45. Loebel A, Tsodyks M (2002) Computation by ensemble synchronization in recurrent networks with synaptic depression. *J Comput Neurosci* 13:111–124.
46. Polsky A, Mel B, Schiller J (2004) Computational subunits in thin dendrites of pyramidal cells. *Nat Neurosci* 7:621–627.
47. Dayan P, Abbott L (2001) *Theoretical Neuroscience: Computational and Mathematical Modeling of Neural Systems* (MIT Press, Cambridge, MA).
48. Holmgren C, Harkany T, Svennenfors B, Zilberter Y (2003) Pyramidal cell communication within local networks in layer 2/3 of rat neocortex. *J Physiol* 551:139–153.
49. Csicsvari J, Hirase H, Mamiya A, Buzsáki G (2000) Ensemble patterns of hippocampal CA3-CA1 neurons during sharp wave-associated population events. *Neuron* 28: 585–594.
50. Schmitz D, et al. (2001) Axo-axonal coupling: A novel mechanism for ultrafast neuronal communication. *Neuron* 31:831–840.
51. Mercer A, Bannister A, Thomson A (2006) Electrical coupling between pyramidal cells in adult cortical regions. *Brain Cell Biol* 35:13–27.
52. Boss B, Turlejski K, Stanfield B, Cowan W (1987) On the numbers of neurons in fields CA1 and CA3 of the hippocampus of Sprague-Daley and Wistar rats. *Brain Res* 406: 280–287.
53. Buhl E, Szilágyi T, Halasy K, Somogyi P (1996) Physiological properties of anatomically identified basket and bistratified cells in the CA1 area of the rat hippocampus in vitro. *Hippocampus* 6:294–305.
54. Jonas P, Major G, Sakmann B (1993) Quantal components of unitary EPSCs at the mossy fibre synapse on CA3 pyramidal cells of rat hippocampus. *J Physiol* 472:615–663.
55. Liu G, Tsien R (1995) Properties of synaptic transmission at single hippocampal synaptic boutons. *Nature* 375:404–408.
56. Angulo M, Rossier J, Audinat E (2001) Postsynaptic glutamate receptors and integrative properties of fast-spiking interneurons in the rat neocortex. *J Neurophysiol* 82:1295–1302.
57. Hájos N, Mody I (1997) Synaptic communication among hippocampal interneurons: Properties of spontaneous IPSCs in morphologically identified cells. *J Neurosci* 17: 8427–8442.
58. Pearce R (1993) Physiological evidence for two distinct $GABA_A$ responses in rat hippocampus. *Neuron* 10:189–200.
59. Bartos M, Vida I, Frotschner M, Geiger J, Jonas P (2001) Rapid signaling at inhibitory synapses in a dentate gyrus interneuron network. *J Neurosci* 21:2687–2698.

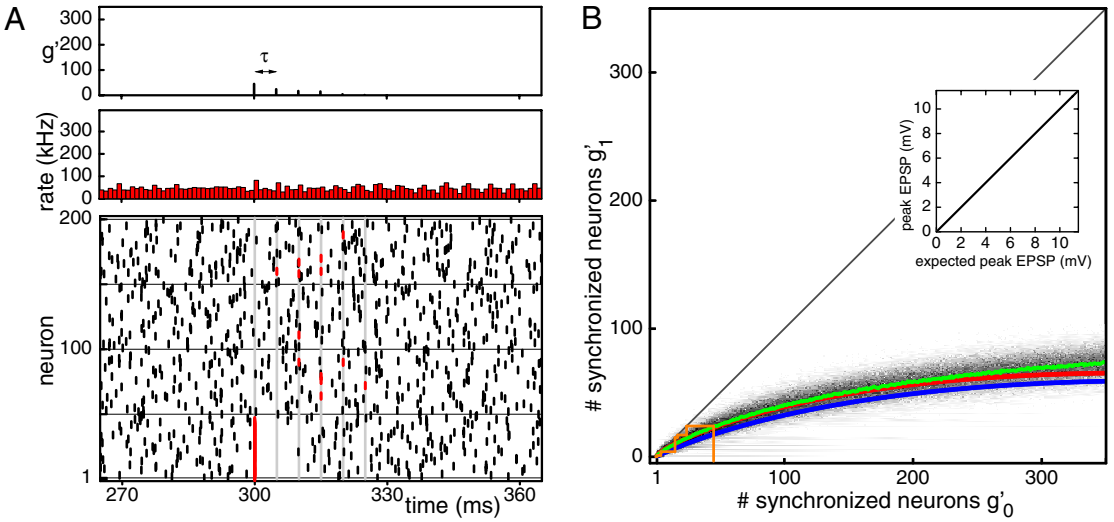

Fig. S1. Random networks with linear coupling do not generate transiently increased activity and high-frequency oscillations. (*A*) A section of the dynamics of a linearly coupled network with a synchronous pulse of size $g'_0 = 45$ generated at time $t_0 = 300$ ms by external stimulation. This initiates a short-lived chain of decaying synchronous pulses. (*Bottom*) Spiking activity of 200 neurons; spikes within the chain are marked in red. (*Middle*) The network's spike rate (bin size 1 ms). (*Top*) The size of synchronous spike pulses within the chain. The evolution of the pulse chain can be understood quantitatively in Markovian approximation, as illustrated by *B*. The chain evolution is characterized by the transition matrix (gray shading). The dots (overlapping, forming curves) indicate the mean response pulse sizes derived numerically (green), semianalytically (red), and analytically (blue). The orange lines illustrate the evolution of the event in *A*. *Inset* displays the dendritic modulation function σ (black line).

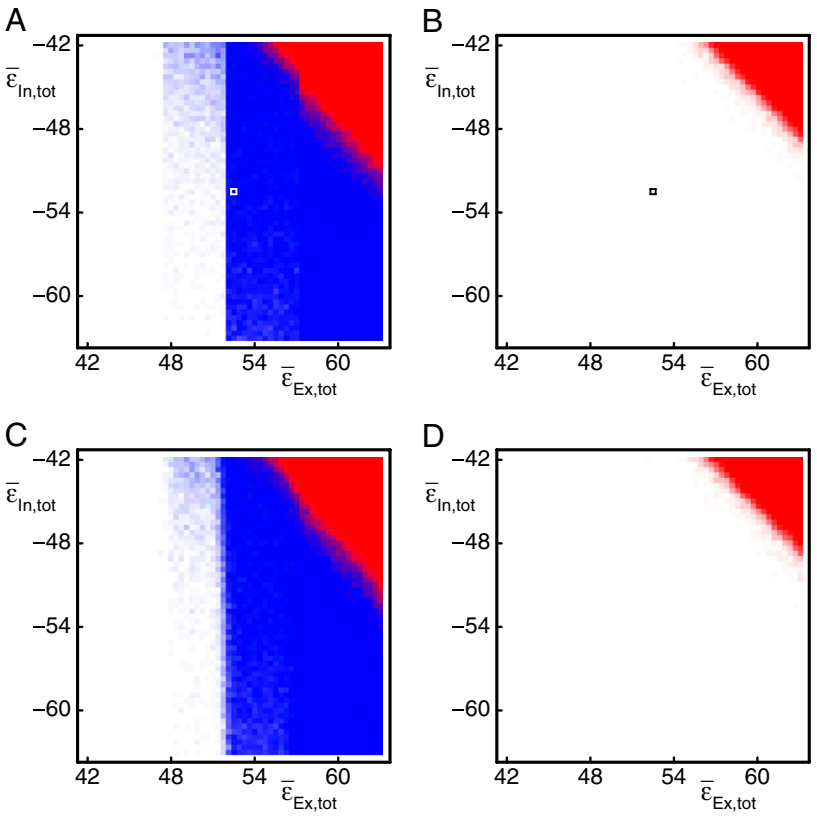

Fig. S2. Short-lived, enhanced propagation of synchrony occurs in networks incorporating supralinear dendritic interactions over large parameter ranges (*A* and *C*) in contrast to linearly coupled networks (*B* and *D*). Chains of propagating synchrony are initiated by external stimulation of synchronous groups of $g_0^{\prime}$ = 45 neurons in supralinearly (*A* and *C*) and linearly (*B* and *D*) coupled networks with homogeneous (*A* and *B*) and inhomogeneous (*C* and *D*) coupling strength distribution. The mean excitatory and inhibitory coupling strengths are varied. Blue areas indicate the occurrence of short-lived, enhanced propagation of synchrony which is present over large parameter ranges in supralinearly coupled networks (*A* and *C*). Red indicates unstable background activity. The white square in *A* and the black square in *B* highlight the coupling strengths used for the networks in Fig. 1 and Fig. S1, respectively.

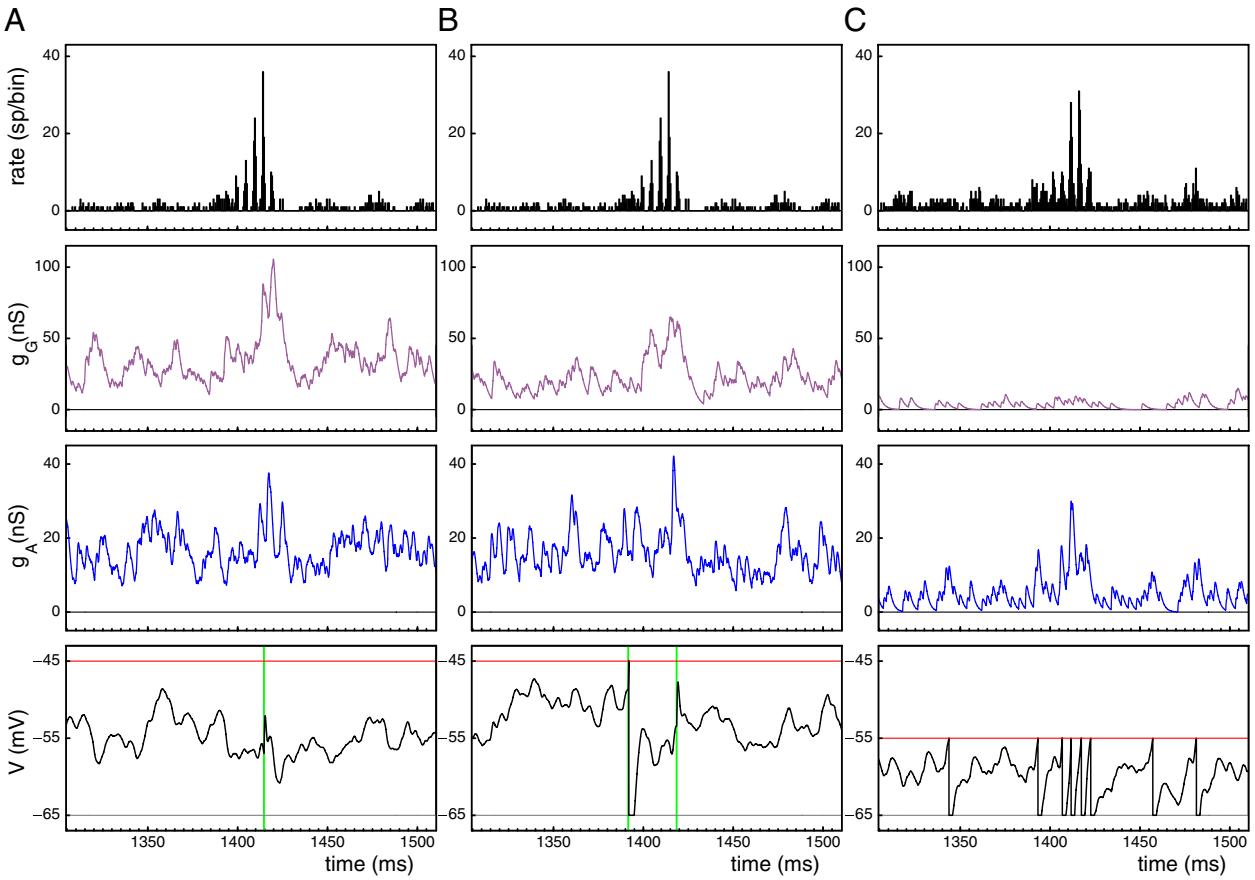

Fig. S3. Single-neuron dynamics during a phase of increased activity with high-frequency oscillations. *A* and *B* show the dynamics of excitatory neurons, and *C* shows the dynamics of an inhibitory neuron. From top to bottom, the rows display the spike rate of the associated neuron population (number of spikes per 0.5-ms bin), the conductance of the inhibitory synapses at the neuron, the conductance of the excitatory synapses at the neuron, and the neuron's membrane potential.

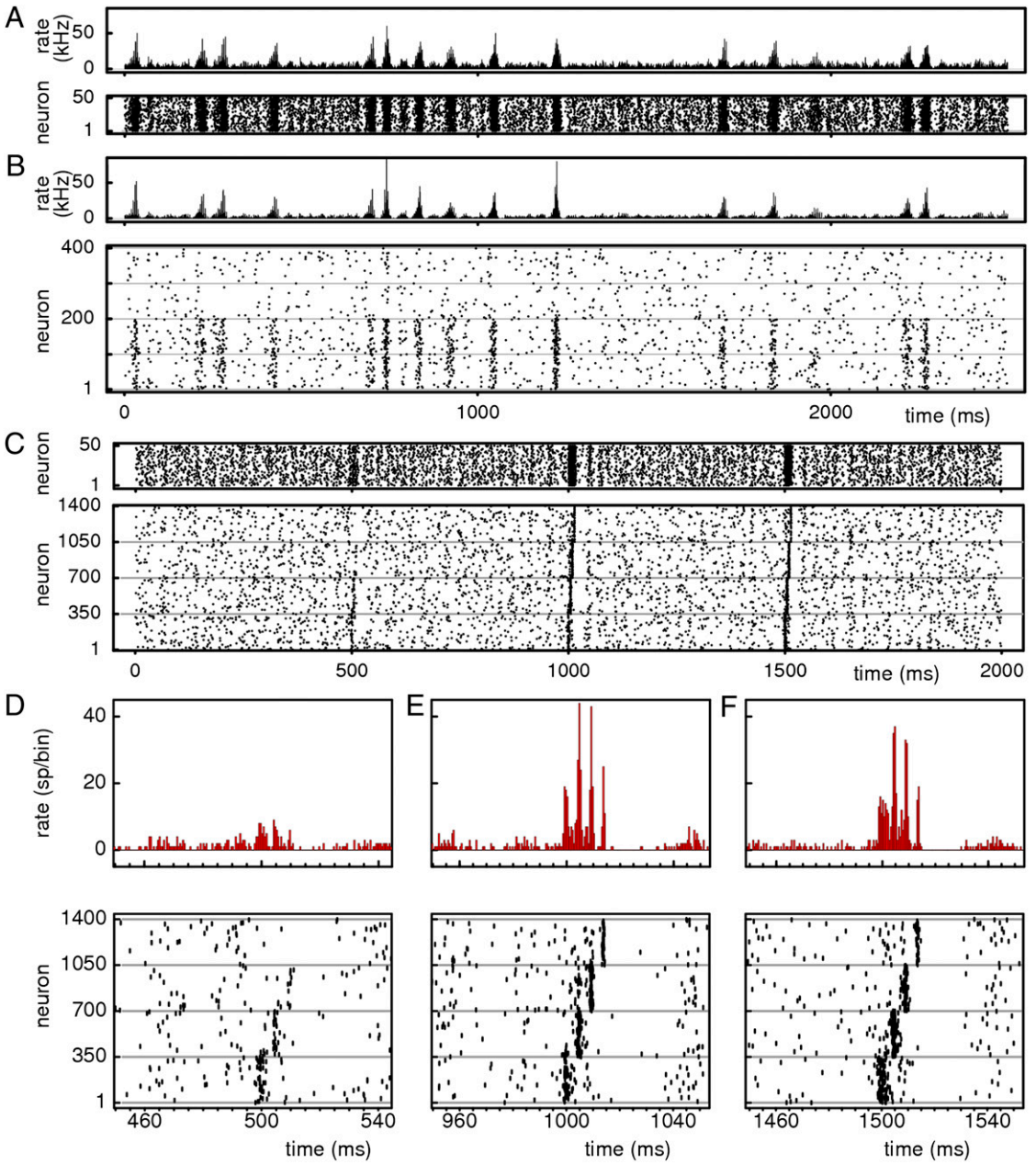

Fig. S4. Spiking dynamics in structured networks. *A* and *B* show the spiking dynamics of a network with a subpopulation of excitatory neurons whose recurrent connections allow supralinear dendritic interactions. *A* shows the rate (*Upper*) and the spiking activity of a part (*Lower*) of the inhibitory population. *B* shows the rate (*Upper*) and the spiking activity of a part (*Lower*) of the excitatory population. *C–F* show the spiking dynamics of a network with a sequence of groups of excitatory neurons whose connections from one group to the next allow supralinear dendritic interactions. *C* shows the spiking activity of a part of the inhibitory population (*Upper*) and of the excitatory population (*Lower*). *D–F* show the spiking activity (*Lower*) and the rate (*Upper*) of the excitatory population during events.

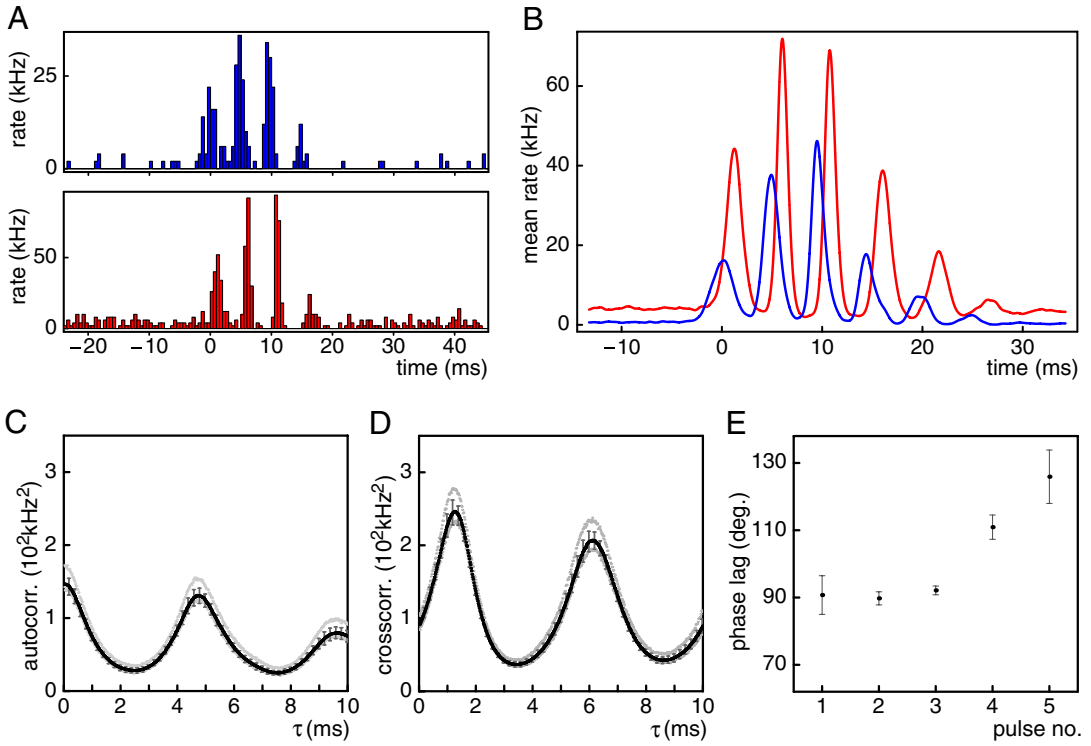

Fig. S5. Phase relationship between the excitatory and the inhibitory neuron populations in a model incorporating fast interneurons during events of increased activity with high-frequency oscillations. *A* displays the rates of the excitatory population (*Upper*; blue) and of the inhibitory population (*Lower*; red) during a single event. *B* shows the average rate taken over all events in a trial. *C* shows the autocorrelation of the rate of the excitatory neuron population, and *D* shows the cross-correlation of the rates of the excitatory and the inhibitory neuron populations. *E* displays the averaged phase lag of the inhibitory population rate with respect to the excitatory population rate during events.

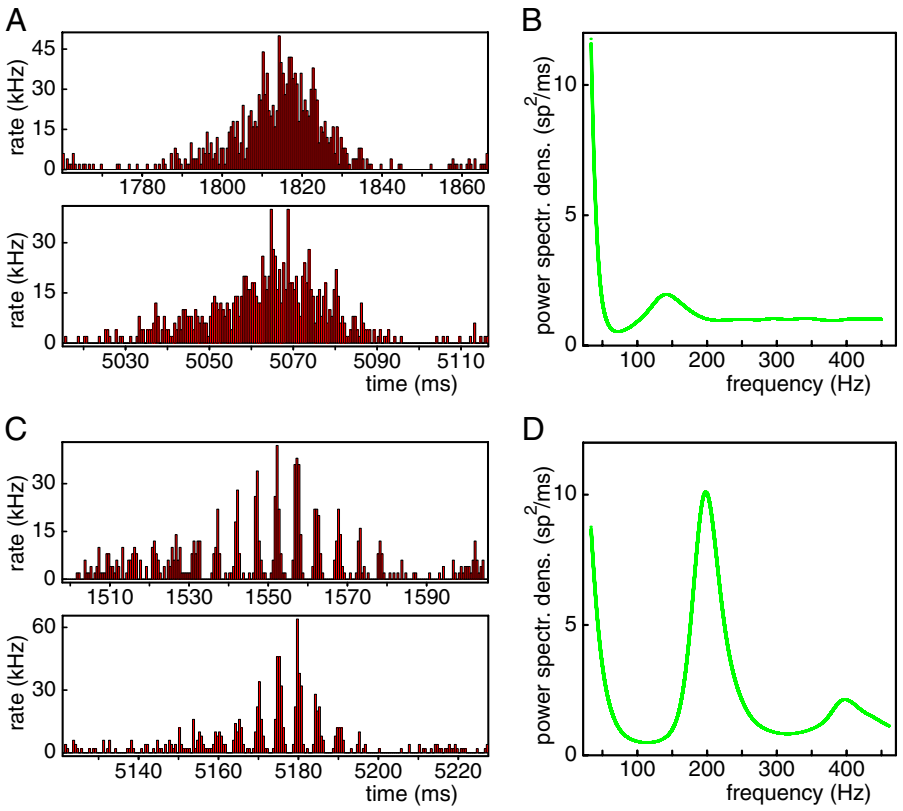

Fig. S6. Long and broadly distributed axonal conduction delays lead to smoothing of oscillations and to a decrease in the oscillation frequency. *A* shows the rate (bin size 0.5 ms) of the excitatory neuron population during two single events (*Upper* and *Lower*) for a network with long and broadly distributed delays. *B* shows the power spectrum of the rate of the excitatory population. For comparison, *C* and *D* show the corresponding results for a network with reduced mean and width of the delay distribution.

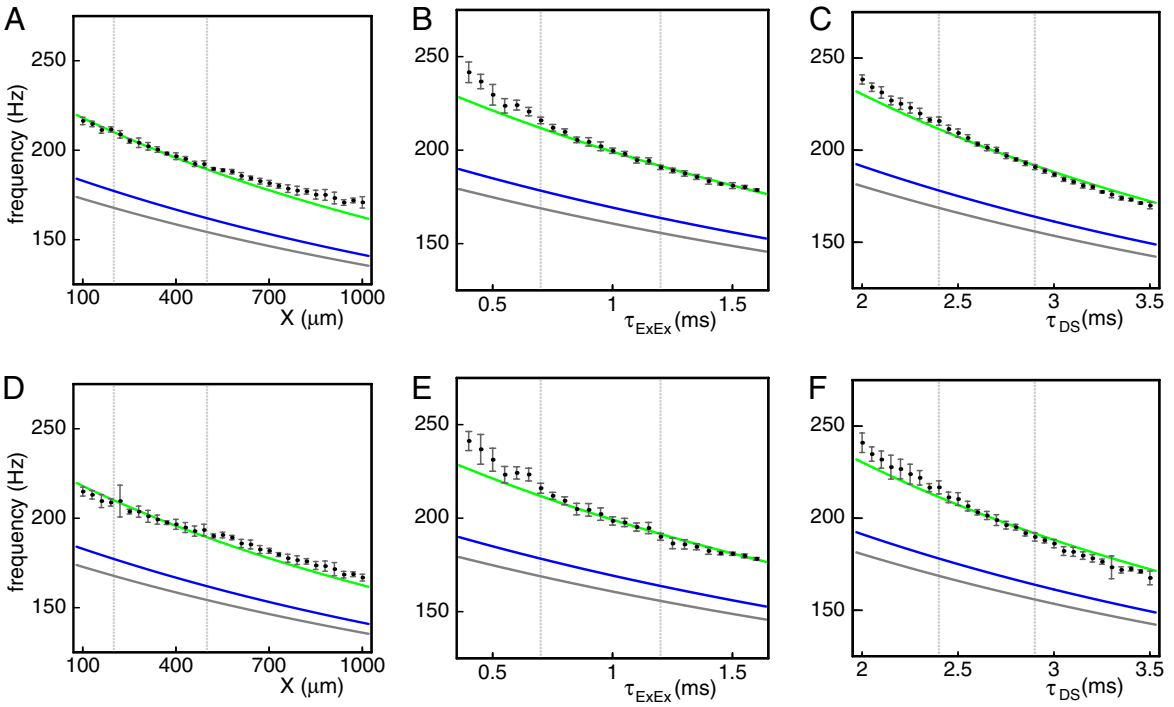

Fig. S7. The leading frequency of intermittent high-frequency oscillations is about 200 Hz even if the network parameters are varied over broad ranges. The figure shows the leading frequency dependent on the spatial extent of the network X (*A* and *D*), dependent on the synaptic (and dendritic) delay τ_{ExEx} (*B* and *E*), and dependent on the time τ_{DS} from the onset of the somatic AMPA response to the somatic response to the dendritic spike (*C* and *F*). The green curves show the frequency dependence in model 1. The black dots show numerical results for model 2 for the excitatory (*A*–*C*) and for the inhibitory (*D*–*F*) population. Error bars indicate the SD of the distribution. The blue and gray curves display results from an analytical low-frequency approximation (*SI Text*). Biologically plausible parameter ranges for region CA1 are highlighted by light gray dashed lines.

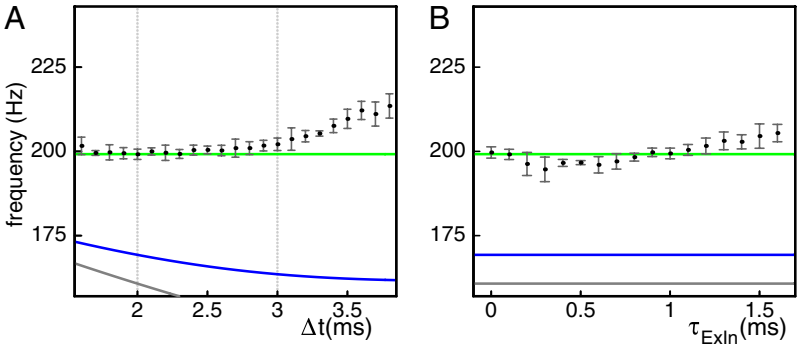

Fig. S8. The dependence of the oscillation frequency on the window for supralinear interaction and on the timing of inhibitory feedback is weak. The figure displays the leading oscillation frequencies of the excitatory population dependent on (*A*) the window for supralinear interaction Δt and on (*B*) the synaptic and postsynaptic delay τ_{ExIn} from inhibitory to excitatory neurons. The frequency scale is enlarged compared with Fig. S7. Gray dashed lines indicate the experimentally determined range of Δt for reliable amplification (5). In model 2, the frequency depends only weakly on the parameters (black dots in *A*; error bars indicate size of the SD of the distribution), whereas the parameters do not occur in model 1 (green straight lines). The blue and gray curves show the results from a low-frequency approximation. (See *SI Text* for further details.)

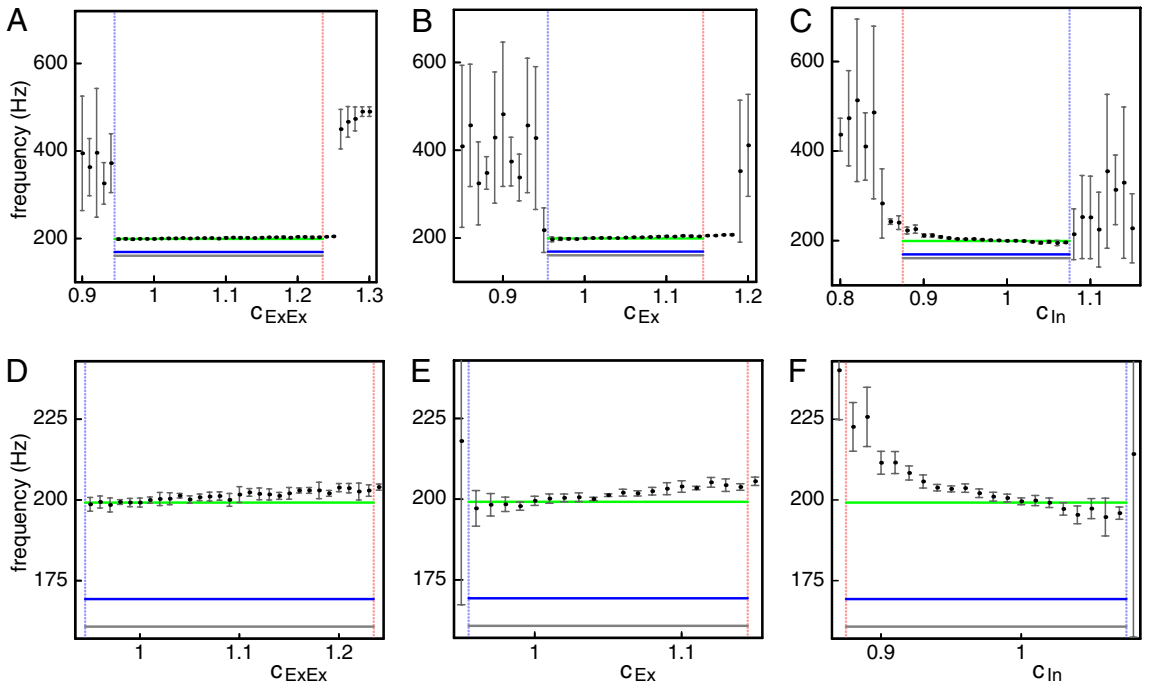

Fig. S9. The dependence of the oscillation frequency on the coupling strengths is weak. The figure displays the leading oscillation frequencies of the excitatory population dependent on (*A* and *D*) the factor c_{ExEx}, scaling the strengths of couplings within the excitatory neuron population, (*B* and *E*) the factor c_{Ex}, scaling all excitatory couplings (internal and external), and (*C* and *F*) the factor c_{In}, scaling all inhibitory couplings (internal and external). Intermittent increases of activity with high-frequency oscillations are reliably present for the range of factors within the red and blue dashed lines; close-ups are shown in *D*–*F*. Within this range, the predictions of model 1 (green straight lines) and of model 2 (black dots; error bars indicate SD of the distribution) agree well. Events in networks near the border of pathological high-frequency activity are markedly increased. The events occur as a nearly continuous chain. (See *SI Text* for further details.)